The 5th Joint International Conference on Multibody System Dynamics
June 24 – 28, 2018, Lisboa, Portugal

Multibody modelling of a flexible 6-axis robot dedicated to robotic machining

Hoai Nam Huynh[1], Edouard Rivière-Lorphèvre[2] and Olivier Verlinden[1]

[1] *Department of Theoretical mechanics, Dynamics and Vibrations, University of Mons, Belgium,*
HoaiNam.Huynh@umons.ac.be, Olivier.Verlinden@umons.ac.be
[2] *Department of Machine Design and Production Engineering, University of Mons, Belgium,*
Edouard.RiviereLorphevre@umons.ac.be

ABSTRACT — *As robots are increasingly involved in industry, robotic manufacturing techniques arise in order to replace their conventional counterpart. Advances in robotics led to improvements in the robot internal mechanics and in their control to be able to address more challenging applications such as friction stir welding, jet cutting, casting, etc... Robotic machining is also one of them as there is still much research to be done in the area. Combining the agility and the flexibility of the industrial robot, this economical solution may represent an alternative for finishing operations, especially for large workpieces coming from aeronautics or foundry industry. Nevertheless, robotic machining encounters some limitations coming from the lack of joint stiffness which influence the positioning accuracy of the cutting tool. This paper focusses on the modelling aspects of a flexible industrial robot compelled to machining operations. The latter was modelled as a multibody system comprising six degrees of freedom whose end-effector carried a payload representing the spindle holding the cutting tool. Moreover, each axis was supplemented with torsional springs and dampers to capture the joint and drive flexibilities. Milling forces were then computed and applied at the tool tip. Robot dimensions were recovered from CAD models and were used to analytically compute its inverse kinematics. After a description of the robotic machining environment, the paper compares cutting force results coming from model variants taking into account different effects such as gravity and backlash. Simulated milling operations are conducted in aluminium and steel along a straight line toolpath and results are compared with experimental data.*

1 Introduction

Robotic machining represents large cost savings for companies willing to rework their manufactured parts. The use of an industrial robot as a machine tool is particularly interesting for milling operations on large parts as the cost of a CNC machine increases according to its size. This technology combines the robot agility and flexibility resulting in a large workspace and achievable complex machining operations. Robotic milling solutions are also valued for their ability to perform convoluted toolpath trajectory infeasible in conventional CNC milling. Common applications are found in foundry industry [1] and in aeronautics [2] for pre-machining, machining, finishing, drilling and the deburring of large parts [3]. However, robotic machining still struggles to establish its position on the market as its working area mainly covers low force applications. As a matter of fact, industrial robots are typically configured as open kinematic chains which encompass less joint stiffness [4]. Their relatively low structural stiffness compared to CNC machine tool is a major drawback when high cutting forces are involved. In this situation, induced process vibrations propagate along the kinematic chain decreasing the machining accuracy if one of the robot natural frequencies is excited. This phenomenon of self-excited vibrations, called mode-coupling chatter, often appears when inappropriate cutting parameters are selected or when excessive cutting forces are applied [5]. Consequently, a better understanding of phenomena appearing in robotic machining is required in order to avoid or cancel chatter.

Many research topics around robotic machining are currently open to improve the milling accuracy which was reported near 0.25 mm under process loads of 100 N [6]. The study of the robot dynamic behaviour is carried by the joint stiffness identification. The elastostatic model can be identified through modal analysis [7, 8] or by applying loads at the end effector and measuring the deflections [9]. Experimental measurements usually locate the first robot natural frequencies below 100 Hz. On the other hand, the robot configuration and the workpiece placement is also important [10, 11]. Dealing with milling stability using robots feeds lots of robotic machining research in order to find the chatter symptoms. For example, chatter online detection for robotic boring process is studied by means of the Hilbert-Huang transform [12]. Authors also propose several models to highlight the phenomena triggering. Pan et al. [5] built a lumped mass model comprising flexible joints and rigid bodies that could capture the robot low frequencies without the machining frequencies. Mousavi et al. [13, 14] presented two models: the first one with only joint flexibilities and the second one with both joint and robot link flexibilities. It was thereafter demonstrated the interest of considering both while dealing with the stability issue in robotic machining. Other research is focussed on error compensations by relying on adaptive force control [15], offline techniques [16] or online actuation [17].

This paper deals with the building of a flexible robot modelling combined with milling. A project about robotic machining was recently launched at the university of Mons (Belgium) aiming to find the best set of cutting parameters considering the trade off between productivity, accuracy and stability. For this purpose, the robotic machining environment must comprise the prediction of the cutting forces, the updating of the machined surface, the joint compliance and the modelling of actuators and controllers. At this stage of development, machining operations can be virtually conducted by a robot model comprising joint compliances. The first section of this article will be devoted to the development of the robotic machining environment, highlighting the robot modelling. Different options of robot modelling are presented taking successively into account a gravity compensation, orthogonal compliance and backlash. The milling model and its coupling with the robot model will then be briefly explained. A benchmark milling operation will then be presented for the purpose of achieving a shoulder milling operation in aluminium and steel. The simulation results are finally shown in terms of cutting force amplitudes, roughness and machined part shapes and are compared with their experimental counterpart.

2 Robotic machining environment

This first section aims to present the robotic machining environment which results from the coupling of an in-house multibody library `EasyDyn` [18] and an in-house milling routine `Dystamill` [19]. Figure 1 presents the robotic machining setup consisting of a 6-axis robot equipped with a spindle achieving a shoulder milling operation. The workpiece is clamped on a force sensor in order to measure cutting forces along the three orthogonal directions. The illustrated operation will be discussed throughout the article considering a plate in aluminium and then in steel.

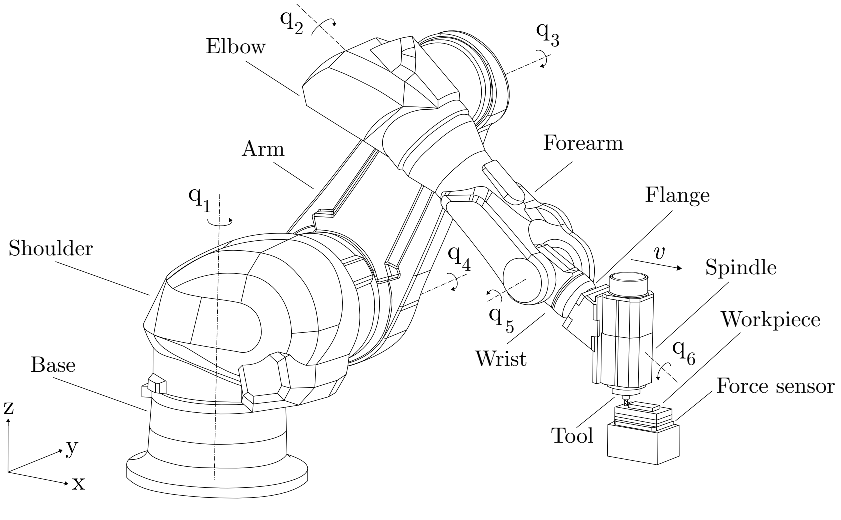

Fig. 1: 6-axis industrial robot: Stäubli TX200 robot

2.1 Robot modelling

Continuing the work achieved in [20] in which an industrial robot was modelled as a simplified multibody system with four degrees of freedom, the model was extended in order to take into account its six degrees of freedom. The multibody approach was chosen since it allows large translational and rotational displacements for its body motion as opposed to the finite element or the lumped mass methods. Therefore, the usage of `EasyDyn` seemed necessary to keep the mastery and the scalability of the in-house library. Furthermore, the connection with the milling routine `Dystamill` had to be ensured as well.

In `EasyDyn`, the set of configuration parameters $\underline{\mathbf{q}}$ is freely chosen according to the minimal coordinate formalism. The configuration of each body must be expressed as a 'one-to-one' relationship in terms of the configuration parameters, which implies that they are independent. It also means that the number of configuration parameters is equal to the number of degrees of freedom. When using the multibody library, the user writes a `C++` application in which the kinematics of all bodies is gathered in a routine called `ComputeMotion()`. The latter contains the expressions of position and orientation, associated velocities and accelerations for each body i in terms of the configuration parameters $\underline{\mathbf{q}}$ and their first and second time derivatives $\underline{\dot{\mathbf{q}}}$ and $\underline{\ddot{\mathbf{q}}}$. At the same time, the user specifies all the forces applied on the bodies through another specific routine `AddAppliedForces()`. From the system kinematics and the expressions of the applied forces, the n_{cp} equations of motion binding n_B bodies and the n_{cp} configuration parameters can be built from the application of the d'Alembert's principle

$$\sum_{i=1}^{n_B}[\underline{\mathbf{d}}^{i,j}\cdot(\underline{\mathbf{R}}_i - m_i\underline{\mathbf{a}}_i) + \underline{\boldsymbol{\theta}}^{i,j}\cdot(\underline{\mathbf{M}}_{G_i} - \boldsymbol{\Phi}_{G_i}\underline{\dot{\boldsymbol{\omega}}}_i - \underline{\boldsymbol{\omega}}_i \times \boldsymbol{\Phi}_{G_i}\underline{\boldsymbol{\omega}}_i)] = 0 \quad j = 1,\dots,n_{cp} \tag{1}$$

with

- m_i and $\boldsymbol{\Phi}_{G_i}$: the mass and the central inertia tensor of body i;
- $\underline{\mathbf{R}}_i$ and $\underline{\mathbf{M}}_{G_i}$: the resultant force and torque at the centre of gravity G_i applied on body i;
- $\underline{\mathbf{a}}_i$: the acceleration of the centre of gravity of body i;
- $\underline{\mathbf{d}}^{i,j}$: the partial contributions of $\dot{q}_j$ in the velocity $\underline{\mathbf{v}}_i$ of the centre of gravity of body i: $\underline{\mathbf{v}}_i = \sum_{j=1}^{n_{cp}} \underline{\mathbf{d}}^{i,j}\cdot\dot{q}_j$;
- $\underline{\boldsymbol{\theta}}^{i,j}$: the partial contributions of $\dot{q}_j$ in the rotational velocity $\underline{\boldsymbol{\omega}}_i$ of body i: $\underline{\boldsymbol{\omega}}_i = \sum_{j=1}^{n_{cp}} \underline{\boldsymbol{\theta}}^{i,j}\cdot\dot{q}_j$.

The corresponding equations of motion can then be reduced to the following compact and classical form

$$\mathbf{M}(\underline{\mathbf{q}})\cdot\underline{\ddot{\mathbf{q}}} + \underline{\mathbf{h}}(\underline{\mathbf{q}},\underline{\dot{\mathbf{q}}},t) = 0 \tag{2}$$

comprising the $n_{cp} \times n_{cp}$ mass matrix $\mathbf{M}$ and $\underline{\mathbf{h}}$ collecting the centrifugal, Coriolis and gyroscopic effects and the contribution of the applied forces.

A convenient way to handle the expression of the kinematics of each body is to use the homogeneous transformation matrix $\mathbf{T}_{0,i}$, expressing the position and orientation of body i with respect to body (coordinate system) 0 (Fig. 2). Practically, this matrix is expressed as the multiplication of typical matrices, corresponding to the successive elementary motions along a kinematic chain

$$\mathbf{T}_{0,i} = \mathbf{T}_{motion_1}\cdot\mathbf{T}_{motion_2}\cdot\ldots\cdot\mathbf{T}_{motion_l} \tag{3}$$

in which $\mathbf{T}_{motion_k}$ is the kth elementary motion (translation/rotation along/around one axis).

The homogeneous transformation matrix $\mathbf{T}_{i,j}$ comes in the general form of a 4×4 matrix

$$\mathbf{T}_{i,j} = \begin{pmatrix} \mathbf{R}_{i,j} & \{\underline{\mathbf{r}}_{j/i}\}_i \\ 0\,0\,0 & 1 \end{pmatrix} \tag{4}$$

where $\{\underline{\mathbf{r}}_{j/i}\}_i$ is the coordinate vector between frames i and j projected in frame i and $\mathbf{R}_{i,j}$ is the rotation matrix reflecting the orientation of frame j relatively to frame i.

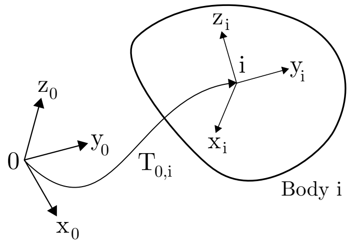

Fig. 2: Frame situation of body i with respect to the global reference frame 0

The Stäubli TX200 robot is used as an illustrative example throughout the article. As suggested earlier, it is a 6-axis robot comprising six revolute joints connecting seven links. The name of the links is illustrated in Fig. 1. From bottom to top, the base link is connected to the shoulder link through a revolute joint about the z-axis, the latter is linked with the robot arm by a y-axis revolute joint and is hooked up with the elbow by a rotational joint about the y-axis. The end point of the kinematic chain forms a spherical wrist (rotation motion around the three orthogonal axes) involving the three last linkages: the forearm, the wrist and the flange. The Stäubli TX200 robot is a heavy payload robot able of supporting nominal loads of 100 kg for a maximum reach of 2194 mm.

The direct kinematics, i.e. the expression of the robot end effector position and orientation from the joint angles, were established using the homogeneous transformation matrix formalism. For each link, a transformation homogeneous matrix was built in order to position and orientate its centre of mass. For the sake of simplicity, the initial configuration is selected as depicted in Fig. 3, arm deployed vertically as referenced in the robot manufacturer datasheet (zero-encoder pose). Since the joint and centre of mass position are confidential data, authors relied on computer-aided designs (CAD) supplied by the robot manufacturer. However, the original CAD's were all solid shapes without the representation of the interior of the parts. In order to further identify the mass and inertia properties, and to locate the centre of mass of each link, it was decided to redesign each part on the basis of photographs of the robot interior. The mass of each component could be calculated after the assignation of the material (aluminium or steel if magnetizable). Knowing that the total robot weight is 1000 kg, the 3D representation was also enriched with the inclusion of motor and gearbox masses based on their real dimensions in order to get a realistic distribution of the robot mass. Once the 3D modelling of the robot completed, a convention was adopted to locate the centre of mass of each component. The latter is positioned by a vector $\underline{\text{AG}}$ starting from the entry flange of the link towards its centre of mass. The outer flange of the link is then measured from the centre of mass through vector $\underline{\text{GB}}$.

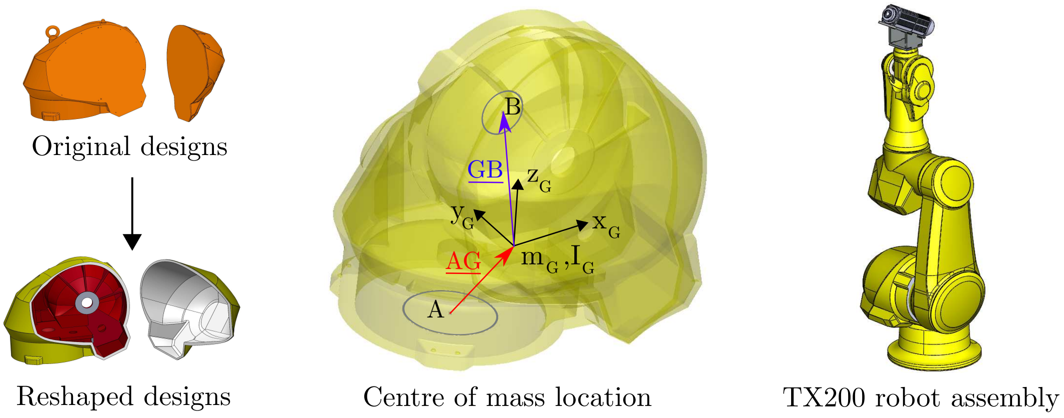

Original designs

Reshaped designs

Centre of mass location

TX200 robot assembly

Fig. 3: Modelling steps of the robot model

All kinematic data for the positioning of the centres of mass and joints are gathered in Table 1 according to the adopted convention relative to the motion flange of each link.

Centre of mass position	$\underline{AG}_{Base}$	$\underline{AG}_{Shoulder}$	$\underline{AG}_{Arm}$	$\underline{AG}_{Elbow}$	$\underline{AG}_{Forearm}$	$\underline{AG}_{Wrist}$	$\underline{AG}_{Flange}$
x [m]	0.007	0.150	0.007	0.039	0	0	0
y [m]	0.001	-0.008	0.139	-0.219	0.004	0	0
z [m]	0.119	0.209	0.401	-0.043	0.266	0.068	0.005

Joint position	$\underline{GB}_{Base}$	$\underline{GB}_{Shoulder}$	$\underline{GB}_{Arm}$	$\underline{GB}_{Elbow}$	$\underline{GB}_{Forearm}$	$\underline{GB}_{Wrist}$	$\underline{GB}_{Flange}$
x [m]	-0.007	0.100	-0.007	-0.039	0	0	0
y [m]	-0.001	0.243	-0.095	-0.060	-0.004	0	0
z [m]	0.225	0.089	0.549	0.222	0.355	0.109	0.012

Tab. 1: Centre of mass and joint positions for Stäubli TX200 robot (obtained from reshaped CAD)

For illustrative purposes, the homogeneous transformation matrix representing the location of the robot base centre of mass can be expressed as

$$\mathbf{T}_{0,1} = \mathbf{T}_{\text{disp}}(\underline{AG}_{Base}) \tag{5}$$

and the shoulder centre of mass is defined relatively to the base ($\mathbf{T}_{0,1}$) as

$$\mathbf{T}_{1,2} = \mathbf{T}_{\text{disp}}(\underline{GB}_{Base}) \cdot \mathbf{T}_{\text{rotz}}(q_1) \cdot \mathbf{T}_{\text{disp}}(\underline{AG}_{Shoulder}) \tag{6}$$

where $\mathbf{T}_{\text{rot}i}(\theta)$ represents a rotation of an angle θ about local i axis and $\mathbf{T}_{\text{disp}}(\underline{\mathbf{PM}})$ a displacement (without rotation) of a vector $\underline{\mathbf{PM}}$ (projected in local axes). Frame 0 is chosen at the bottom of the base as depicted in Fig. 4 which also highlights the frame situating the joint pivot point. Approximated joint positions were derived from CAD flange limits and from the robot manufacturer datasheet.

Whereas the homogeneous transformation matrix formalism was useful to locate the positions of the centres of mass and joints for the direct kinematics, the Denavit-Hartenberg convention was deployed to solve the complete inverse kinematics analytically. The inverse kinematics of an industrial robot consists in finding its joint angles from a desired end effector pose, obviously leading to several possible configurations (eight for an anthropomorphic industrial robot). The Paul's method was implemented to solve the inverse kinematics problem for the six angles. The method decomposes the problem in two steps: it is first asked to compute the three first joint angles positioning the wrist and then to solve the three last Euler angles (zyz) orienting the wrist [21]. Consequently, a common practice in robotics is to provide the Denavit-Hartenberg parameters positioning uniquely the pivot points of a kinematic chain as for example for the Stäubli TX200 robot in Tab. 2. In this article, the standard convention is adopted (Fig. 5).

Motion axis: θ [rad]	d [m]	a [m]	α [rad]
θ_1	0.642	0.25	$-\pi/2$
θ_2	0	0.95	0
θ_3	0	0	$\pi/2$
θ_4	0.8	0	$-\pi/2$
θ_5	0	0	$\pi/2$
θ_6	0	0	0

Tab. 2: Stäubli TX200 standard Denavit-Hartenberg parameters

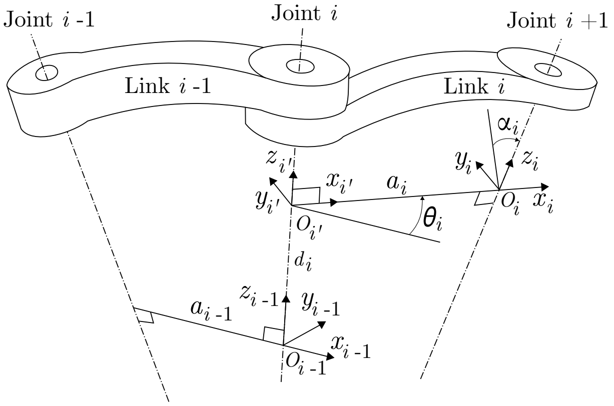

Fig. 5: Standard Denavit-Hartenberg convention [22]

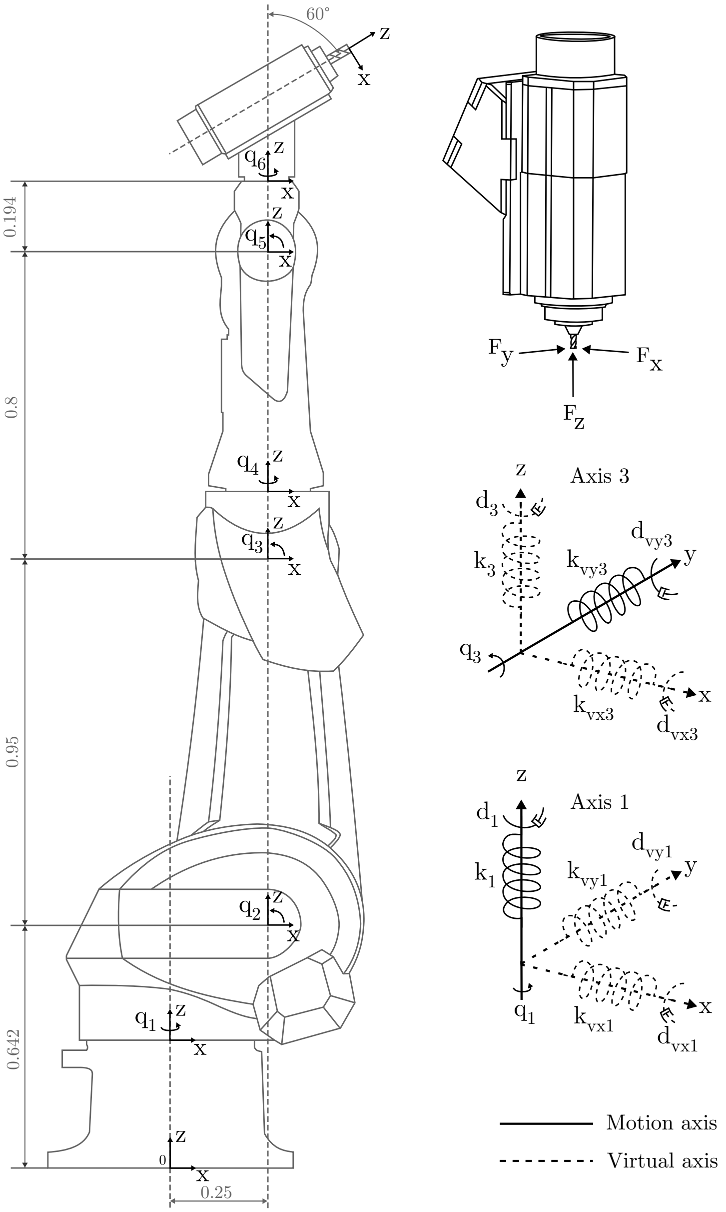

Fig. 4: Stäubli TX200 robot dynamic multibody model

To conclude with the kinematics of the milling robot, it is also necessary to position and orientate the tool centre point (TCP) defining the tip of the cutting tool. It is determined using the same methodology as for the robot links by passing through the centre of mass of the spindle from the robot flange $\underline{AG}_{Payload}$. The TCP is then localized using vector $\underline{GB}_{Payload}$ (Tab. 3). Although the robot flange frame is oriented in the same way as frame 0, it is preferred to align the z-axis of the TCP frame with the tool axis, (outwards direction) reachable by a $\mathbf{T}_{\text{roty}}(60^\circ)$.

Centre of mass position	$\underline{AG}_{Payload}$	TCP position	$\underline{GB}_{Payload}$
x [m]	-0.004	x [m]	0.205
y [m]	0	y [m]	0
z [m]	0.158	z [m]	0.159

Tab. 3: Centre of mass of the spindle ($\underline{AG}_{Payload}$) and TCP position ($\underline{GB}_{Payload}$)

As previously announced, the redesign of the robot CAD's not only provided the centre of mass and joint position but also the mass and inertia properties. In Tab. 4, the components of the inertia tensor are defined at the centre of mass of each link. The mass of the payload comprises the mass of the spindle plus its steel support. An ATC71 Teknomotor spindle was mounted on the robot end effector for the experimental tests.

	Base	Shoulder	Arm	Elbow	Forearm	Wrist	Flange	Payload
Mass [kg]	226	364	256	99	41	14	0.6	44.4
I_{xx} [kg.m^2]	8.30	12.25	36.58	0.57	1.23	0.03	6e-3	0.095
I_{yy} [kg.m^2]	7.98	17.83	39.92	0.51	1.17	0.03	6e-3	0.106
I_{zz} [kg.m^2]	11.87	16.95	6.57	0.46	0.30	0.02	1e-3	0.098
I_{xy} [kg.m^2]	0	-0.20	0.05	-0.02	0	0	0	0
I_{xz} [kg.m^2]	-0.01	1.55	0.18	-0.07	0	0	0	0.035
I_{yz} [kg.m^2]	0	0.25	0.74	0.02	0.06	0	0	0

Tab. 4: Stäubli TX200 dynamic parameters at the centre of mass for each robot links (obtained from reshaped CAD)

To address the stability issue in robotic milling, it is necessary to take into account the robot flexibility. In this article, joint and drive flexibilities are considered through torsional springs and dampers located at the joints. The basic robot model only incorporated rotational flexibilities around the motion axes as reported in Fig. 4. Given that the motion of the virtual robot needed information concerning the torques acting on the joints, their computation had to be included in the modelling. Since no information on the drive/gearbox nor the control strategy was known, it was assumed that each motor was at its desired position θ_i. The spring and damper system was located just after the motor, thus modifying the value of the configuration parameter q_i through the spring stiffness k_i and a damping d_i. In the absence of backlash in the gearbox, the torque acting on one motion axis is computed as follows

$$\tau_i = k_i \cdot (q_i - \theta_i) - d_i \cdot \dot{q}_i. \tag{7}$$

Stiffness values were borrowed from an ABB IRB6660-205/1.9 robot (Tab. 5). In [23], the identification of its model parameters for individual joints is carried out without disassembling the robot. Whereas its payload is almost the double relatively to the Stäubli TX200 robot, ABB IRB6660-205/1.9 has the same workspace and is often studied for milling applications in the literature.

Joint stiffness [Nm/rad]	Joint 1	Joint 2	Joint 3	Joint 4	Joint 5	Joint 6
	2.03e6	6.02e6	1.91e6	0.45e6	0.22e6	0.07e6

Tab. 5: ABB IRB 6660-205/1.9 joint stiffness borrowed for the robot modelling

Concerning the joint damping, as their values are harder to find in the literature, a proportional formula was derived as follows

$$d_i = 0.05 \cdot d_{ref} \cdot \sqrt{\frac{k_i}{k_{ref}}} \tag{8}$$

which requires the knowledge of one set of stiffness k_{ref} and damping values d_{ref}. A square root was added to mimic the formula of the critical damping coefficient and a weighting factor of 0.05 was inserted to not overdamp the system with purely real poles. Reference values for joint stiffness k_{ref} and damping d_{ref} were found in [24] allowing the deduction of the joint damping values (Tab. 6).

Joint damping [Nms/rad]	Joint 1	Joint 2	Joint 3	Joint 4	Joint 5	Joint 6
	383.3	660	371.7	180.5	126.2	71.2

Tab. 6: Joint damping values for the robot modelling

From the above information, a first modelling of the Stäubli TX200 robot was built in `EasyDyn` comprising the joint flexibilities without considering the effect of gravity.

2.1.1 Gravity compensation

A particular feature of the Säubli TX200 robot is the inclusion of a preloaded spring inside the arm (third link) which greatly alleviates the torque required by its second motor. This gravity compensation is especially useful when the whole structure is outstretched horizontally. Since no information is given by the robot manufacturer concerning the spring stiffness, the gravity compensation was implemented by applying additional joint torques computed from the cantilevered lever arms. Knowing the positions of the centre of mass for all the links as well as their respective mass, the joint torques were calculated to compensate the load supported by axes 2, 3 and 5 when subjected to the gravity field. For example, to compensate the gravity forces exerted on the robot wrist without any payload (i.e. without spindle) at axis 5, the cancelling torque can be expressed as

$$\tau_{5,gravity} = \underline{\mathrm{AG}}_{Wrist}\ sin(q_2+q_3+q_5)\cdot \mathrm{m}_{Wrist}\cdot g + (\underline{\mathrm{AG}}_{Wrist} + \underline{\mathrm{GB}}_{Wrist} + \underline{\mathrm{AG}}_{Flange})\ sin(q_2+q_3+q_5)\cdot \mathrm{m}_{Flange}\cdot g \quad (9)$$

with g the earth's gravity taken as 9.81 m/s^2 and m_{Wrist} and m_{Flange}, the masses of the wrist and the flange, respectively. Similar expressions were derived to compensate the gravity effects for axes 2, 3 and 5 and this improvement constituted a second model variant.

2.1.2 Joint orthogonal flexibility

As suggested by some authors, only considering flexibility around the axes of motion might not be sufficient to completely capture all low frequency mode shapes of the robot [7, 16]. Consequently, the joint stiffness model was enhanced using the so-called Virtual Joint Method (VJM) adding two more rotational degrees of freedom for each joint [25]. Virtual springs and dampers were appended around axes orthogonal to the motion axes later called virtual axes as depicted in Fig. 4. The latter aim at representing the limited torsional stiffness of the gearboxes while the links are assumed to be stiff. Orthogonal joint torques were therefore computed to take into account the torsional flexibilities. If the motion axis lies along the z-axis, orthogonal joint torques are applied around axes x and y as follows

$$\tau_{x|y,i} = k_{v\,x|y,i}\cdot(q_{x|y,i}-0) - d_{v\,x|y,i}\cdot\dot{q}_{x|y,i}. \quad (10)$$

which is similar to Eq. 7 excepted that the desired position is null. Values for all orthogonal stiffness k_v and damping d_v are freely chosen at 5e6 Nm/rad and 1000 Nms/rad, respectively.

Kinematically, accounting for flexibilities orthogonal to the motion axis introduces additional degrees of freedom. For instance, for the rotational motion of the shoulder around the z-axis, the position of its centre of mass can be rewritten as

$$\mathbf{T}_{1,2} = \mathbf{T}_{\mathrm{disp}}(\underline{\mathrm{GB}}_{Base})\cdot\mathbf{T}_{\mathrm{rotz}}(q_1)\cdot\mathbf{T}_{\mathrm{rotx}}(q_{x,1})\cdot\mathbf{T}_{\mathrm{roty}}(q_{y,1})\cdot\mathbf{T}_{\mathrm{disp}}(\underline{\mathrm{AG}}_{Shoulder}). \quad (11)$$

By following this approach for all the motion axes, this third robot model variant ended up with 18 degrees of freedom including flexibilities around motor axes and orthogonal to the latter.

2.1.3 Backlash modelling

The last robot model variant included a representation of the backlash as proposed in [16]. Backlash was only taken into account around motion axes. For this purpose, equation giving the joint torques (Eq. 7) was slightly modified with the incorporation of the backlash s_i chosen identically for all axes

$$\tau_i = -d_i \cdot \dot{q}_i + k_i \cdot \begin{cases} ((q_i - s_i) - \theta_i) & \text{, if } (q_i - \theta_i) \geq s_i \\ ((q_i + s_i) - \theta_i) & \text{, if } (q_i - \theta_i) \leq -s_i \\ 0 & \text{, else.} \end{cases} \tag{12}$$

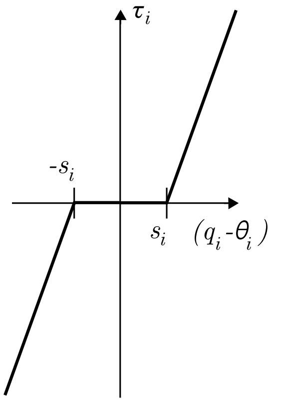

Fig. 6: Backlash model

This representation introduces the backlash non-linear behaviour by imposing null torques when gear teeth are not in contact, typically when the joint direction of rotation is changing. Backlash values were chosen knowing that a common order of magnitude is the arc second and to further match the experimental cutting force trend: s_i = 15 arcsec = 7.3 e-5 rad.

2.2 Milling model

The computation of the milling forces is based on a model developed for machine tool simulations. It was established to study the stability of milling operations [26]. The milling model relies on a macroscopic approach to predict the cutting forces which are applied on the mechanical system under the form of force elements. Once the tool centre position under the process forces is known, the shape of the machined part is updated by removing the corresponding chip section. Milling routines are gathered in an in-house library called `Dystamill` which offers the possibility to study the stability of operations in $2D^{1/2}$ such as slotting, contouring, pocketing or shoulder milling. Complex tool geometry are supported as long as the tool displacement lies in a plane perpendicular to its own axis. The motion of cutting edges is naturally considered to deduce the chip thickness.

For the sake of detecting milling instabilities, it is necessary to model the machined surface as accurately as possible. Indeed, chatter phenomenon is a regenerative process appearing when the tool removes material from a previously machined surface. Dystamill implements an "eraser of matter" model which represents the part as superimposed slices whose contours are approximated by a succession of straight segments as depicted in Fig. 7. The end mill is also discretised into superimposed discs along its revolving axis in such a way that each of them interacts with one 2D contour. User is then free to define the axial depth of cut a_p, the radial depth of cut a_e and the spindle speed Ω of the simulated milling operations.

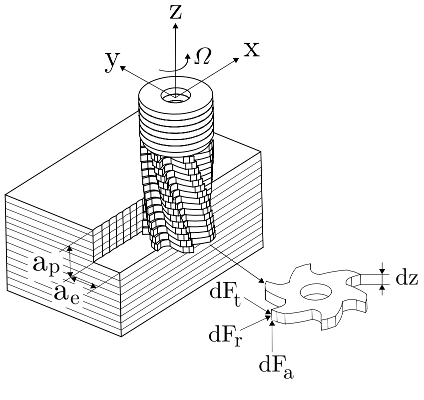

Fig. 7: Milling model

The computation of the cutting forces is based on a so-called mechanistic model. Assuming that the cutting forces are proportional to the local chip thickness h, this type of modelling allows their prediction from a given tool/material couple defining the proportionality coefficient. The latter is often called the specific pressure or simply cutting force coefficient $K_{i,c}$, i defining the direction of the force: radial, tangential and axial.

Cutting force coefficients can be experimentally determined by inverse analysis from slotting operations [27]. As proposed in [28], elementary cutting forces dF_i are calculated for each cutting edge and for each slice representing the workpiece as

$$\begin{cases} dF_t = K_{t,c} \cdot h \cdot db \\ dF_r = K_{r,c} \cdot h \cdot db \\ dF_a = K_{a,c} \cdot h \cdot db \end{cases} \tag{13}$$

with db, the length of elementary segment dz, defined in Fig. 7, projected along the local tangent of the cutting edges.

All elementary contributions of the local cutting forces from Eq. 13 are then summed together for all teeth n_z and for all slices n_e in order to obtain the global cutting forces $F_{x,y,z}$ projected into the global reference frame such as

$$\begin{bmatrix} F_x \\ F_y \\ F_z \end{bmatrix} = \sum_{e=1}^{n_e} \sum_{j=1}^{n_z} [\mathbf{B}] \begin{bmatrix} dF_t \\ dF_r \\ dF_a \end{bmatrix} \tag{14}$$

with $[\mathbf{B}]$ the transformation matrix projecting the local forces into the reference frame and expressed as

$$[\mathbf{B}] = \begin{bmatrix} -cos(\theta) & -sin(\theta) \cdot sin(\kappa) & -sin(\theta) \cdot sin(\kappa) \\ sin(\theta) & -cos(\theta) \cdot sin(\kappa) & -cos(\theta) \cdot cos(\kappa) \\ 0 & -cos(\kappa) & -sin(\kappa) \end{bmatrix} \tag{15}$$

with θ and κ the rotation angle of the cutting edge and the angle orienting the radial direction, respectively.

2.3 Coupling

In order to simulate the whole robotic machining process, it was necessary to couple the milling routine with the robot model built in the multibody framework `EasyDyn`. Prior bridging the two in-house frameworks into one coupled environment, classical machine tool test cases were carried out and validated on the basis of cutting force results [29]. Figure 8 presents the interactions between the milling routine and the multibody framework. The initialization of the multibody and machining processes is the entry step to simulate a robotic machining operation: all the kinematics and the dynamic properties of the multibody system as well as the cutting conditions must be defined (tool diameter $\varnothing_{\text{tool}}$, number of teeth n_z, etc...). Once the simulation parameters are loaded, the inverse kinematics procedure allows computing the robot joint angles thus positioning the TCP at the desired location in the Cartesian space. From the TCP position inside the material, a chip thickness can be computed through an intersection procedure between the cutting edges and the contours of the workpiece. Consecutively, global cutting forces are inferred from the chip thickness and applied on the mechanical system as force elements through the integration procedure.

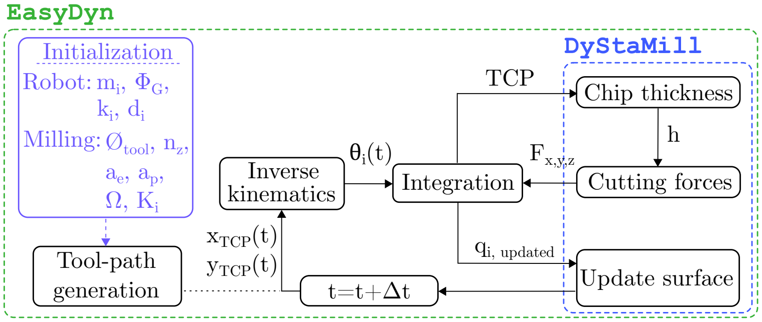

Fig. 8: Robotic machining simulation environment

In this simulation environment, the Newmark integration scheme, with its classical parameters α=0.25 and β=0.5, is chosen to optimize energy preservation. The Newmark integration formulas are written

$$\begin{cases} q^{t+h} = q^t + h\dot{q}^t + (0.5-\beta)h^2\ddot{q}^t + \beta h^2\ddot{q}^{t+h} \\ \dot{q}^{t+h} = \dot{q}^t + (1-\gamma)h\ddot{q}^t + \gamma h\ddot{q}^{t+h} \end{cases} \tag{16}$$

where β and γ are the Newmark parameters, h being the integration time step. Once the convergence is reached for all the configuration parameters taking the milling forces into account, the workpiece surface can be updated by removing the machined chip. The milling procedure is resumed by providing a new Cartesian position for the TCP thus feeding the inverse kinematics.

3 Simulation example: shoulder milling operation

As announced earlier, the robotic machining environment was used to simulate two shoulder milling operations, first in aluminium 6060 T6 and then in steel St 52-3. This short section aims to provide the disposition of the two tests by supplying the robot configuration and the cutting conditions.

3.1 Robot configuration

Shoulder milling operations were carried out so that the TCP remains in a horizontal plane (Fig. 1); the same trajectory parameters were kept for the two operations. The robot starts its motion outside the workpiece and then follows the x-axis with a constant velocity while milling over a workpiece length of 90 mm. The motion of the TCP was settled so that its velocity increased smoothly from a null speed to the desired feed rate by tuning the jerk parameter. Although the figure presents the robot in an outstretched configuration to get familiar with its component, the machined workpiece is closer to the robot base forcing its arm to be slightly folded up as shown in Fig. 9. Initial robot configuration is given in Tab. 7.

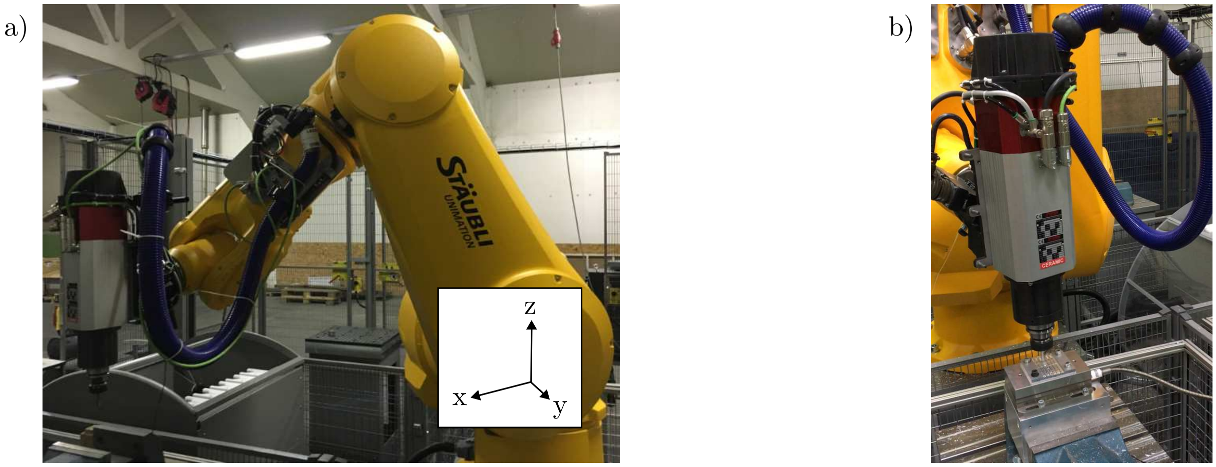

Fig. 9: a) Robot initial configuration before milling - b) Milling of an aluminium plate

Initial joint positions [°]	Joint 1	Joint 2	Joint 3	Joint 4	Joint 5	Joint 6
	-11.71	20.78	-212.14	82.76	60.80	-166.96

Tab. 7: Robot initial configuration before milling

3.2 Aluminium 6060 T6 milling

Cutting parameters were chosen in accordance to the preliminary experimental tests and originally from the recommendations of the tool manufacturer. Selected parameters are shown in Tab. 8 for the operation in aluminium, using the down-milling direction. A particular feature from the tool was that its teeth were not equally spaced (variable tooth pitch) to prevent self-excited vibrations. The tool/material couple was identified by prior slotting tests in the same material and the same robot leading to the following cutting coefficients $K_{t,c}$ = 661.553 MPa and $K_{r,c}$ = 253.458 MPa; $K_{a,c}$ was not identified as the axial signal is often of a lesser quality.

Solid tool	Diameter [mm]	10	*Milling operation*	Radial depth of cut [mm]	4
	Nb. of teeth	2		Axial depth of cut [mm]	1.6
	Helix angle [°]	30		Spindle speed [RPM]	18700
	Variable tooth pitch [°]	170-190		Feed rate [mm/min]	3700

Tab. 8: Milling parameters for the shouldering operation in aluminium (down-milling)

3.3 Steel St 52-3 milling

Similarly, cutting parameters for the operation in steel were the same as in the experiment (Tab. 9). This time, one of the teeth was slightly longer than the other leading to a small runout expressed in micron. Identified cutting coefficients were the followings $K_{t,c}$ = 3333 MPa and $K_{r,c}$ = 2289 MPa.

Solid tool	Diameter [mm]	10	*Milling operation*	Radial depth of cut [mm]	4
	Nb. of teeth	2		Axial depth of cut [mm]	1.6
	Helix angle [°]	30		Spindle speed [RPM]	3100
	Runout [μm]	6.929		Feed rate [mm/min]	280

Tab. 9: Milling parameters for the shouldering operation in steel (down-milling)

4 Results

The result section concentrates on the cutting force signals retrieved from the simulation of each robot model: without gravity, with gravity compensation, with orthogonal compliance and with backlash. At a first sight, cutting forces will be shown over a duration taking into account the complete shoulder milling operation. A close-up will allow comparing simulated and experimental results. Then, the shapes of the real and simulated machined parts will be examined. Results are first presented for the aluminium and then the steel.

4.1 Aluminium machining

4.1.1 Cutting forces

Let us first take a look at the experimental results in aluminium 6060 T6 for the proposed example (Fig. 10).

The figure displays cutting forces F_x and F_y which correspond to the force along the direction of the TCP motion and the direction of the feed and perpendicular to the direction of the feed, respectively. As it can observed, cutting forces are rather constant over the whole shoulder milling operation, F_x remains around 50 N and F_y stays around -120 N. The cutting force steady state is reached quite rapidly whereas the end of the signals is characterised by a rise of F_x and the decline of F_y. It is due to a small tool deviation at the end of the pass.

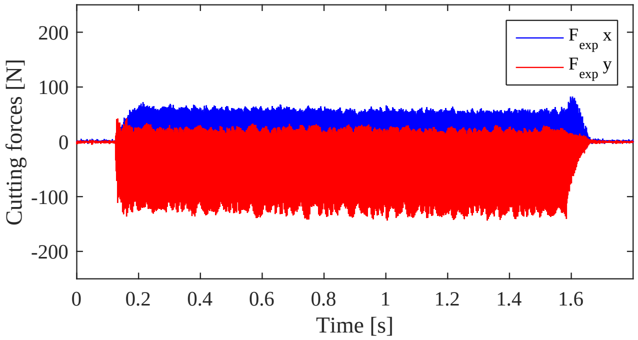

Fig. 10: Experimental cutting forces in aluminium

Robot model without gravity effects

Cutting force results for the robot model only considering flexibilities around axes of motion and without any gravity effects are illustrated in Fig. 11. Globally, cutting force amplitudes are well correlated which means that cutting force coefficients were well identified. Indeed, in Eq. 13, specific pressure coefficients are mainly accountable for the force amplitudes. Despite the lack of noise around the steady state values, rise of cutting forces is abrupt at the beginning of the pass as for the experimental results. At the end of the pass, the model is also able to capture the tool deflection as can be seen from the very small increase of F_x on the close-up of the figure.

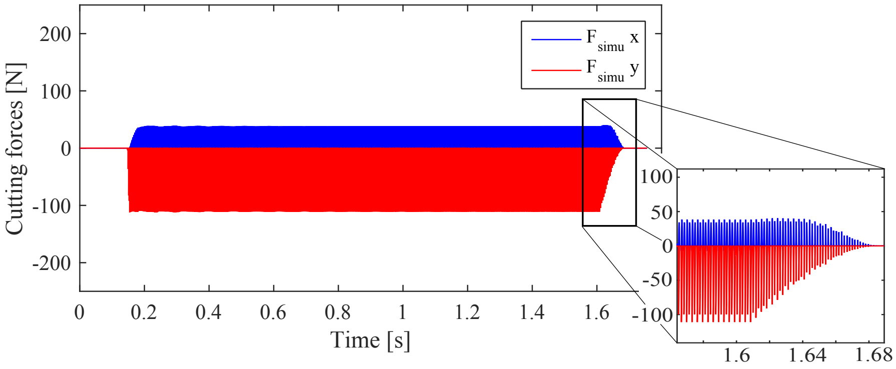

Fig. 11: Cutting forces in aluminium when gravity is deactivated

Robot model with gravity compensation

As might be expected, the inclusion of the feature allowing to compensate gravity effects does not change the overall shape of the cutting forces. It only lightly decreased the torque delivered by the motors. Entry and exit conditions of the machined material are very similar (Fig. 12).

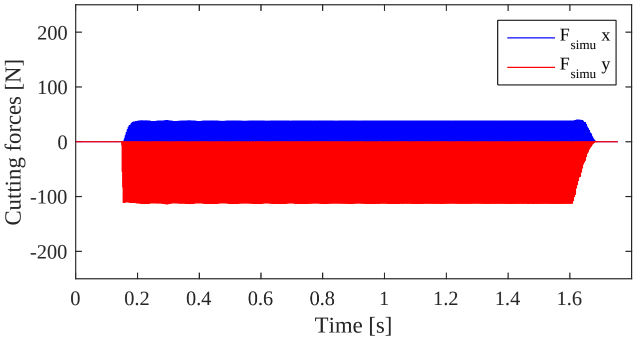

Fig. 12: Cutting forces in aluminium under gravity field and gravity compensation

Robot model with orthogonal flexibilities

The robot model including orthogonal flexibilities besides gravity compensation yielded interesting results in terms of cutting forces. Since the robot became more flexible, cutting force amplitudes started to oscillate around their steady state values. Moreover, the rise in the cutting force F_x at the end of the pass was more observable confirming that the effect comes from the robot joint flexibility.

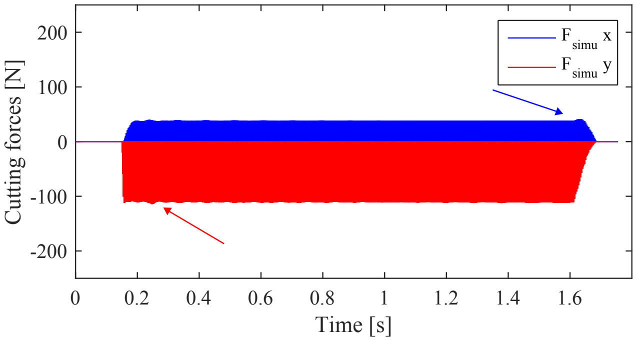

Fig. 13: Cutting forces in aluminium using joint orthogonal flexibility

Robot model with backlash

The final robot model including all the modelled effects (gravity compensation, orthogonal bushing and backlash) was also subjected to the shoulder milling test. As depicted in Fig. 14, the global shape of the cutting force signals starts to really fit the experimental measurements. Backlash effect is somehow activated when cutting forces are applied at the TCP, briefly reversing the rotary motion on some axes. This modelling addendum mainly influences the tool entry in the material. Cutting forces stabilised anyway as long as the TCP slightly deviates from the workpiece until the small F_x rise at the end of the pass.

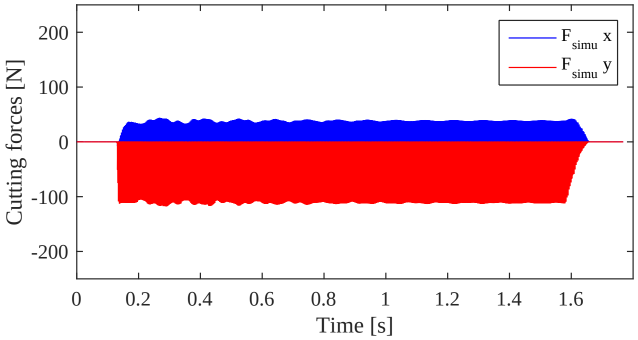

Fig. 14: Cutting forces in aluminium using joint orthogonal flexibility and backlash

Cutting force close-up

A closer look at the cutting forces proves a significant accordance between the experimental (thin lines) and simulated results (bold lines). Both signals are displayed over three tool turns resulting in six peaks as the tool possessed two teeth (Fig. 15). Simulated results come from the robot model including all effects. Furthermore, given that the end mill featured a variable tooth pitch (170°—190°), cutting force amplitudes alternated between higher and lower peaks as it was the case for experimental data, especially visible for F_y.

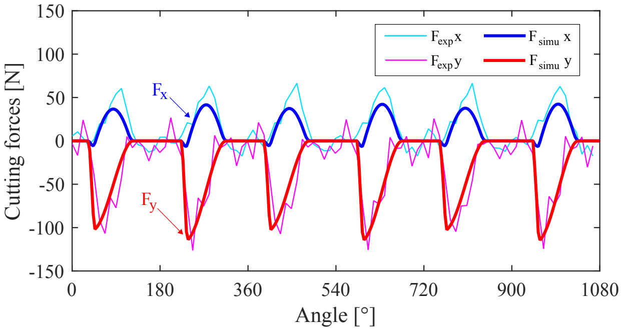

Fig. 15: Zoom over three tool turns for the cutting forces in aluminium

Summary for aluminium milling

As a summary for aluminium milling tests, Tab. 10 provides a comparison of cutting force results in terms of minimum (Min.), maximum (Max.), mean and root mean square (RMS) values. If only the models are considered, computed values seem quite constant for all categories. If experimental data are now included, it is noticed that experimental extrema (in absolute terms) are always higher than the simulated ones. The reason comes from the fact that a low-pass filter is used to identify the cutting force coefficients thus lowering the amplitudes. This effect is particularly visible for the mean and RMS values of cutting force F_x. Regarding cutting force F_y, mean and RMS values are close to the experimental values.

	Min. [N]		Max. [N]		Mean [N]		RMS [N]	
	F_x	F_y	F_x	F_y	F_x	F_y	F_x	F_y
Experimental	-24.66	-143.69	68.11	33.00	15.14	-29.75	27.16	50.45
Basic model	-7.63	-111.39	38.82	0	8.78	-25.67	16.28	44.42
Gravity compensation	-8.53	-113.4	38.84	0	8.72	-26.1	16.31	44.96
Orthogonal compliances	-7.92	-112.45	38.98	0	8.79	-25.70	16.29	44.47
Backlash and compliances	-8.31	-117.07	42.40	0	8.92	-25.43	16.41	44.15

Tab. 10: Comparison of the cutting force levels in aluminium (between 0.4 and 1.4 s)

4.1.2 Surface finish and roughness

Surface finish is also compared with the real machined part. Since the milling routine only allows cutting force computation for planar TCP motions, the roughness of the bottom face could not be assessed. Hence, the comparison is made on the machined lateral face (Fig. 16). At a first glance, both profiles seemed quite smooth and highlighted the deviation of the tool at the end of the pass. The real tool deviation appeared to be somewhat higher than for the simulated part. Along the pass, the simulated profile showed asperities of ± 1 μm which were quite congruent with the real part.

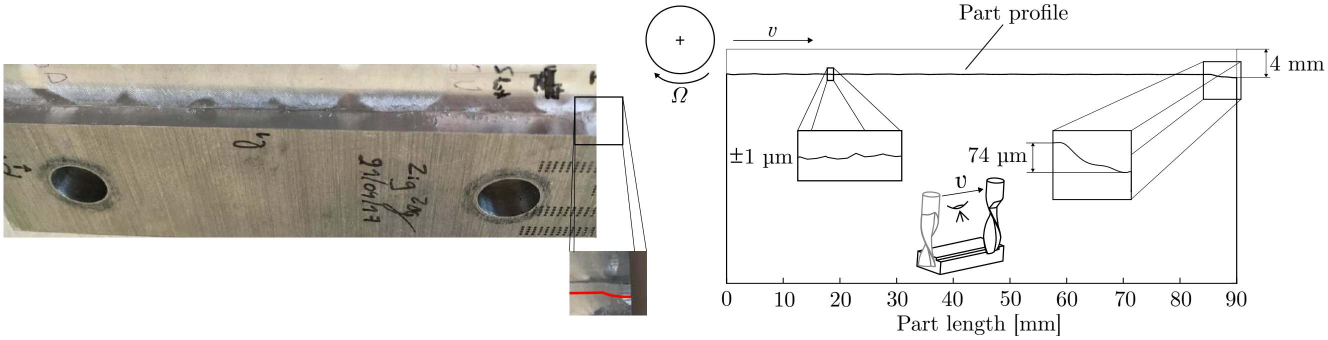

Fig. 16: Experimental and simulated aluminium lateral profile

Table 11 exposes the comparison of roughness values for the lateral face. The three types of roughness are compared as designated by the arithmetic roughness R_a, the quadratic roughness R_q and the total roughness R_t. Experimental measurements provide a range of plausible values which are also well corroborated with the simulated values.

Roughness	simulation	experimental
R_a [μm]	0.37	0.4 - 0.8
R_q [μm]	0.5	0.4 - 0.8
R_t [μm]	13.5	10 - 15

Tab. 11: Comparison of the roughness values for aluminium tests

4.2 Steel machining

4.2.1 Cutting forces

The same analysis was attempted for the machining tests in steel St 52-3. Figure 17 shows the experimental cutting forces for the shoulder milling operation. For an axial depth of cut of 1.6 mm, the stability of milling was preserved and an accentuated tool deviation was observed at the end of the pass. Hence, the presence of a F_x peak can be noticed around 20 s. Cutting forces along x-axis stabilized around 100 N whereas orthogonal cutting forces oscillated around -500 N.

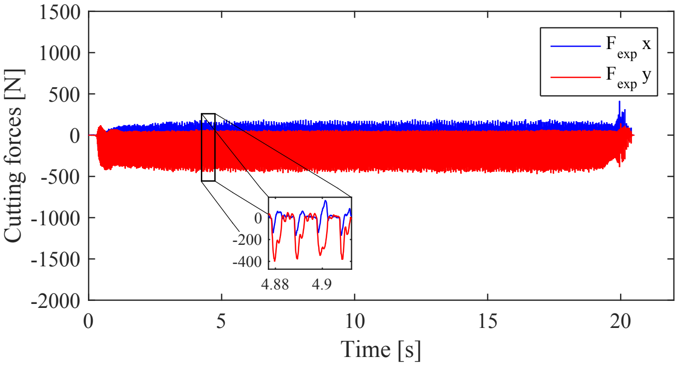

Fig. 17: Experimental cutting forces in steel

Despite a correct identification of the cutting force coefficients, correlation of cutting forces perceived in steel was more challenging. All robot modellings provided unstable results whereas stable cutting forces were measured. Figure 18 presents typical simulated cutting force results, in this case for the model without any gravity effects.

It seems that the material entry happened as in reality but quickly shifted towards an unstable regime. Unstable conditions were characterised by cutting force amplitudes near -2000 N along the orthogonal axis. It is suspected that the robot controller might play a stabilising role. Controller reaction might deliver additional joint torques and possible damping to impose the correct trajectory to its TCP. It was indeed demonstrated that increasing ten times the joint damping while keeping all other parameters unchanged lead to stable results, (Fig. 19).

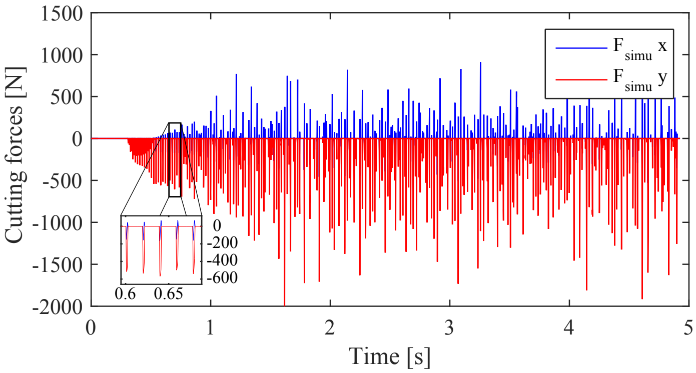

Fig. 18: Cutting forces in steel when gravity is deactivated

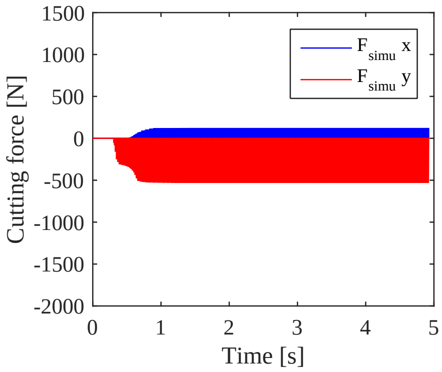

Fig. 19: Cutting forces in steel with increased joint damping

Since cutting force amplitudes retrieved for steel tests were not comparable, it was not relevant to provide the comparison table with min., max., mean and rms values.

4.2.2 Surface finish and roughness

Regardless, the comparison of the lateral profile left by the tool on the real and simulated parts was still carried out (Fig. 20). It appeared that asperities of ± 200 microns appeared on the simulated profile whereas in reality they never exceeded 50 microns. The real steel profile was finally quite smooth.

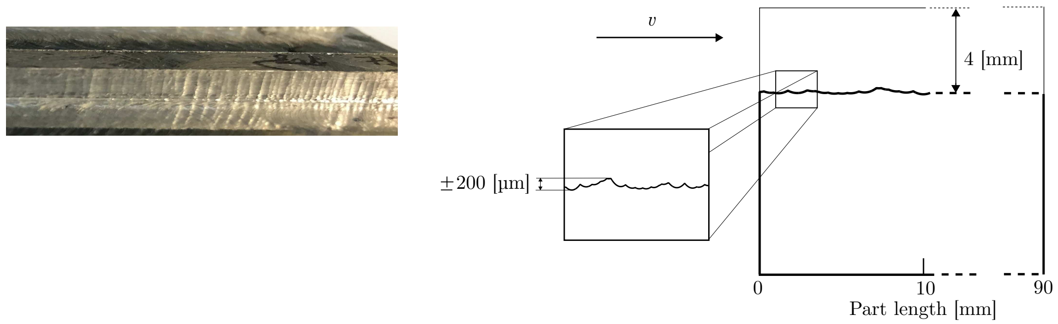

Fig. 20: Experimental and simulated steel lateral profile

Comparison table draws a parallel between experimental and simulated roughness (Tab. 12). Simulated roughness was far above the experimental one given that the simulation was unstable.

Arithmetic roughness	simulation	experimental
R$_a$ [μm]	10.8	0.8 - 5
R$_q$ [μm]	20.9	1 - 10
R$_t$ [μm]	293	3.2 - 50

Tab. 12: Comparison of the roughness values for steel tests

5 Conclusions

Predicting the behaviour of industrial robot under the application of cutting forces is a hot topic for this early century. To that end, a robotic machining simulation environment is being developed and validated at the university of Mons. This paper presented several robot modellings dedicated to milling. The simulated robot was made flexible by the inclusion of torsional springs and dampers localised at the joints. Then, three model variants were proposed to assess the effect of the gravity, the inclusion of orthogonal joint compliances and the influence of backlash. The coupling of the robot model with a milling routine allowed the simulation of robot machining tests. The sensitivity of each model was appraised by simulating a shoulder milling operation, first in aluminium and then in steel. It appeared that the most advanced model, combining the effect of all joint flexibilities and backlash, was able to finely reproduce the cutting force signals and the machined shape of the part for the test in aluminium. In contrast, steel milling was more challenging as simulated results did not match experimental results. Finally, it can be concluded that building a robot model from CADs in the machining context can be sufficient to assess cutting forces of medium amplitudes.

Further investigations will be carried out on the influence of the controller while milling steel and if necessary, a motor and a controller model will be appended to the model. As the university of Mons recently acquired its own Stäubli TX200 robot, identification procedures will be conducted in order to identify its joint stiffness and damping coefficients. Once completed, the robot model will be updated and enhanced in order to study the stability of robotic milling operations. Other perspectives could be the inclusion of flexible bodies to represent the links [30] and the time step extension to decrease the simulation duration [31].

Acknowledgements

The authors would like to acknowledge the Belgian National Fund for Scientific research (FNRS-FRS) for the FRIA grant allotted to H.N. Huynh and CNC Solutions - VDS company for the access granting to their machining robot.

References

[1] F. Leali, M. Pellicciari, F. Pini, G. Berselli and Alberto Vergnonno, "An Offline Programming Method for the Robotic Deburring of Aerospace Components," *Robotics in Smart Manufacturing*, pp. 1–13, 2013.

[2] S. Xie, S. Li, B. Chen and J. Qi, "Research on Robot Grinding Technology Considering Removal Rate and Roughness," *Intelligent Robotics and Applications*, pp. 79–90, 2017.

[3] I. Iglesias, M.A. Sebastian, J.E. Ares, "Overview of the state of robotic machining: Current situation and future potential," *Procedia Engineering*, vol. 132, pp. 911–917, 2015.

[4] S. Baglioni, F. Cianetti, C. Braccesi and D. M. De Micheli, "Multibody modelling of N DOF robot arm assigned to milling manufacturing: Dynamic analysis and position errors evaluation," *Journal of Mechanical Science and Technology*, vol. 30(1), pp. 405–420, 2016.

[5] Zengxi Pan, H. Zhang, "Analysis and Suppression of Chatter in Robotic Machining Process," *International Conference on Control, Automation and systems ICCAS*, pp. 595–600, 2007.

[6] E. Abele, J. Bauer, M. Pischan, O.V. Stryk, M. Friedmann and T. Hemker, "Prediction of the tool displacement for robot milling applications using coupled modes of an industrial robot and removal simulation," *Proceedings of the CIRP 2nd International Conference Process Machine Interactions*, June, 2010.

[7] M. Neubauer, H. Gattringer, A. Müller, A.Steinhauser and W. Höbarth, "A two-stage calibration method for industrial robots with joint and drive flexibilities," *Mechanical sciences*, vol. 6, pp. 191–201, 2015.

[8] P. Glogowski, M. Rieger, J. Sun and B. Kuhlenkötter, "Natural Frequency Analysis in the Workspace of a Six-Axis Industrial Robot using Design of Experiments," *Advanced Materials Research*, vol. 1140, pp. 345–352, 2016.

[9] C. Dumas, S. Caro, S. Garnier, B. Furet, "Joint stiffness identification of six-revolute industrial serial robots," *Robotics and Computer-Integrated Manufacturing*, vol. 27, pp. 881–888, 2011.

[10] S. Caro, C. Dumas, S. Garnier, B. Furet, "Workpiece placement optimization for machining operations with a kuka kr270-2 robot," *IEEE International Conference on Robotics and Automation (ICRA)*, pp. 2921–2926, May, 2013.

[11] J. Li, B. Li, N.Y. Shen, H. Qian and Z. Guo, "Effect of the cutter path and the workpiece clamping position on the stability of the robotic milling system," *Int J Adv Manuf Technol*, vol. 89, pp. 2919–2933, 2017.

[12] G. Wang, H. Dong, Y. Guo and Y. Ke, "Early chatter identification of robotic boring process using measured force of dynamometer," *Int J Adv Manuf Technol*, vol. 94, pp. 1243–1252, 2017.

[13] S. G. Mousavi, V. Gagnol, B.C. Bouzgarou, P. Ray, "Dynamic behaviour model of a machining robot," *ECCOMAS Multibody Dynamics*, pp. 771–779, July, 2013.

[14] S. Mousavi, V. Gagnol, B. C. Bouzgarrou, P. Ray, "Dynamic model and stability prediction in robotic machining," *Int J Adv Manuf Technol (2016), Springer*, pp. 1–13, June 2016.

[15] O. Sörnmo, B. Olofsson, A. Robertsson and R. Johansson, "Increasing Time-Efficiency and Accuracy of Robotic Machining Processes Using Model-Based Adaptive Force Control," *Proceedings of 10th IFAC Symposium on Robot Control*, 2012.

[16] B. Denkena, F. Hollmann, *Process Machine Interactions: Prediction and Manipulation of Interactions between Manufacturing Processes and Machine Tool Structures*. Chap: 11: Analysis of Industrial Robot Structure and Milling Process Interaction for Path Manipulation, pp. 250-263, doi: 10.1007/978-3-642-32448-2, Springer, 2013.

[17] U. Schneider, M. Drust, A. Puzik, A. Verl, "Compensation of errors in robot machining with a parallel 3d-piezo compensation mechanism," *Procedia CIRP*, vol. 7, pp. 305–310, 2013.

[18] O. Verlinden, L. Ben Fékih and G. Kouroussis, "Symbolic generation of the kinematics of multibody systems in EasyDyn: From MuPAD to Xcas/Giac," *Theoretical and Applied Mechanics Letters*, vol. 3, no. 1, pp. 013012, doi: 10.1063/2.13013012, 2013.

[19] E. Rivière, E. Filippi, P. Dehombreux, "Forces, vibrations and roughness prediction in milling using dynamic simulation," *Proceedings*, (Fifth International Conference on High Speed Machining (HSM 2006)), Mars, Metz, France 2006.

[20] H.N. Huynh, O. Verlinden, E. Rivière-Lorphèvre, "Robotic machining simulation using a simplified multibody model," *Proceedings of the 28th DAAAM International Symposium, Published by DAAAM International, ISSN 1726- 9679, DOI: 10.2507/28th.daaam.proceedings.123*, vol. 28, November 2017.

[21] W. Khalil and E. Dombre, *Modeling, identification and control of robots*. Butterworth-Heinemann, 2004.

[22] B. Siciliano, L. Sciavicco, L. Villani, G. Oriolo, *Robotics: Modelling, Planning and Control*. Springer, 2010.

[23] M. Cordes and W. Hintze, "Offline simulation of path deviation due to joint compliance and hysteresis for robot machining," *The International Journal of Advanced Manufacturing Technology*, vol. 90, pp. 1075–1083, 2016.

[24] M. Oueslati, "Contribution à la modélisation dynamique, l'identification et la synthèse de lois de commande adaptées aux axes flexibles d'un robot industriel (translated: contribution to the dynamic modelling, the identification and the synthesis of command laws adapted for industrial robot flexible joints)," *PhD Thesis*, L'école Nationale Supérieure d'Arts et Métiers, ParisTech - Centre de Lille, 2013.

[25] A. Pashkevich, A. Klimchik and D. Chablat, "Enhanced stiffness modeling of manipulators with passive joints," *Mech Mach Theory*, vol. 46(5), pp. 662–679, 2011.

[26] E. Rivière, E. Filippi, P. Dehombreux, "Chatter prediction using dynamic simulation," *International Review of Mechanical Engineering (I.RE.M.E.)*, vol. 1, pp. 78–86, 2007.

[27] Rivière-Lorphèvre, E.; Letot, C.; Ducobu, F.; Dehombreux, P. & Filippi, E. , "Dynamic simulation of milling operations with small diameter milling cutters: effect of material heterogeneity on the cutting force model," *Meccanica*, vol. 52, pp. 35–44, 2017.

[28] Y. Altintas, "Manufacturing Automation: Metal Cutting Mechanics, Machine Tool Vibrations and CNC Design," *1st ed., Cambridge University Press, USA*, 2000.

[29] H.N. Huynh, E. Rivière, O. Verlinden, "Integration of machining simulation within a multibody framework: application to milling," *IMSD: The 4th Joint International Conference on Multibody System Dynamics*, Canada, June, 2016.

[30] O. Verlinden, H.N. Huynh, G. Kouroussis and E. Rivière-Lorphèvre, "Modelling flexible bodies with minimal coordinates by means of the corotational formulation," *Multibody System Dynamics*, vol. 42(4), pp. 495–514, 2018.

[31] E. Rivière-Lorphèvre, H.N. Huynh and O. Verlinden, "Influence of the time step selection on the dynamic simulation of milling operation," *The International Journal of Advanced Manufacturing Technology*, vol. 95, pp. 4497–4512, 2018.